

1 How, where and when do radial faults grow near salt diapirs?

2 Alexander J. Coleman¹, Christopher A.-L. Jackson¹, Oliver B. Duffy² and Maria A.
3 Nikolinakou²

4

5 ¹ Basins Research Group (BRG), Department of Earth Science and Engineering, Imperial College,
6 Prince Consort Road, London, SW7 2BP, UK.

7 ² Bureau of Economic Geology, The University of Texas at Austin, University Station, Box X,
8 Austin, TX 78713-7508, USA.

9

10 *Corresponding author: a.coleman14@imperial.ac.uk

11 *Keywords: Salt tectonics, Radial faults, halokinetic sequences, drape folding, diapirism*

12

13 **ABSTRACT**

14 We examine 3-D seismic reflection data from the Santos Basin, offshore Brazil to determine
15 how, where and when do radial faults grow near a sub-circular salt diapir (stock). We show roof
16 stretching alone cannot account for the large heights and lengths of the kilometre-scale radial
17 faults, suggesting stock widening (‘stem push’), a mechanism implied in numerical models but not
18 yet documented in natural examples, played a pivotal role in radial fault formation. We suggest
19 that, when a diapir is covered by a roof, radial faults form in its overburden due to roof stretching,
20 extending no further than the limit of the drape folding. The roof may then be shouldered aside
21 and the faults buried along the stock flanks, exposing these strata to stem push-related stresses that
22 may then reactivate pre-existing or form new radial faults. Radial faults, irrespective of how they
23 formed, may dip-link with or offset one-another as salt continues to rise. We suggest the causal

24 mechanism for radial fault formation will likely change as roof thickness varies during diapirism,
25 with this reflecting the ratio between sedimentation rate and salt volumetric flux. Our findings are
26 likely applicable to other diapirs, helping us not only to interpret the paleo-stress state of salt-
27 bearing sedimentary basins, but also advancing our understanding of fracture distributions,
28 potential fluid flow pathways, and reservoir compartmentalization around salt diapirs in basins
29 where seismic reflection imaging is poor.

30 **1. INTRODUCTION**

31 Sub-circular salt diapirs or ‘stocks’ are ubiquitous in salt-bearing sedimentary basins, and are
32 typically associated with complex fault networks in surrounding country rock. The most common
33 fault networks comprise ‘radial faults’ (i.e. normal faults that extend radially from a stock into
34 flanking strata). Radial faults may control the migration of crustal fluids (e.g. Davison et al., 2000a)
35 and compartmentalise hydrocarbon reservoirs (e.g. Carruthers et al., 2013), and may provide a
36 relatively high-fidelity record of the evolving near-salt stress conditions associated with salt
37 diapirism (cf. Quintà et al., 2012; Nikolinakou et al., 2014; Maerten et al., 2016).

38 Despite being widespread, and geologically and economically important, the origin of radial
39 faults remains unclear. Radial faults in the unpierced roofs above rising stocks are undoubtedly
40 related to outer-arc extension during active rise, herein termed ‘roof stretching’ (Fig. 1A). Roof
41 stretching-related radial faults may nucleate anywhere in, but not necessarily extend fully across,
42 the arched overburden. As a stock pierces its overburden, roof radial faults may be eroded or
43 shouldered aside, and buried along the stock flanks (e.g. Withjack and Scheiner, 1982; Yin and
44 Groshong Jr, 2007; Carruthers et al., 2013). Stretching and shouldering of the roof may occur
45 during ‘drape folding’ in passive diapirism (Giles and Rowan, 2012), or alternatively during active

46 rise driven by regional shortening (Davison et al., 2000b; Dooley et al., 2009; Jackson and Hudec,
47 2017).

48 Radial faults may also form due to a widening stock pushing outwards against its flanking strata
49 (e.g. Bishop, 1978; Fig. 7 in Nikolinakou et al., 2014), herein termed ‘stem push’ (Fig. 1B). Stem
50 push-related radial faults form at the salt-sediment interface where circumferential stretching is
51 greatest and where the horizontal stresses are anisotropic (i.e. $\sigma_H \neq \sigma_h$). Although numerical models
52 suggest stem push is a plausible mechanism to form radial faults (e.g. Nikolinakou et al., 2014),
53 this prediction has never been critically tested using observations from a natural salt diapir, nor
54 have the associated strains been characterised and quantified.

55 Drape folding above a passively rising diapir is typically recorded by Composite Halokinetic
56 Sequences (‘CHS’; Giles and Rowan, 2012), with two end-members recognised – tapered and
57 tabular. Tapered CHS form when the salt is buried by a relatively thick roof, as sedimentation rate
58 outpaces the volumetric flux of salt; in this case, broad, km-scale drape folds form. Tabular CHS
59 form when the salt is at or very near the surface and covered by only a relatively thin roof i.e. the
60 volumetric flux of salt is greater or equal to the sedimentation rate (e.g. Giles and Rowan, 2012;
61 Jackson and Hudec, 2017); in this case, narrow drape folds (< 200 m) form next to the salt-
62 sediment interface. As the diapiric roof is pierced, drape fold-related radial faults are eroded, being
63 buried and only preserved along the flanks (Fig. 1A). In tapered CHS, radial faults are expected to
64 extend greater distances (<1000 m) from the salt due to broader folding compared to tabular CHS
65 (<200 m). It follows that radial faults extending more than a few hundred metres laterally in tabular
66 CHS must have been influenced by stem push or shortening rather than roof stretching, although
67 this has never been critically tested.

68 Here, we test the hypotheses above by identifying CHS and applying quantitative fault analysis
69 around a salt stock imaged in 3-D seismic reflection data from the Santos Basin, offshore Brazil
70 (Fig. 1C). Using this approach, we: (i) link the genetic mechanism of radial fault formation to
71 modes of salt diapirism, and (ii) to the best of our knowledge, for the first time using a natural
72 example, test the validity of the stem push model, using exceptionally well-imaged radial faults
73 flanking and overlying a salt stock (Fig. 2). These data not only allow us to map radial fault-diapir
74 relationships in three-dimensions and constrain their kinematics, but also investigate when, during
75 diapirism, roof stretching and stem push may occur.

76  Insert Fig. 1

77 **2. DATASET AND METHODS**

78 We used 225 km² of a 850 km², Kirchhoff pre-stack time-migrated (PSTM), zero-phase
79 processed, 3-D seismic dataset. Inline and crossline spacing are 14 m and 25 m, respectively. A
80 frequency of c. 15–40 Hz and assumed average velocity of c. 2000 m/s (after Jackson et al., 2014)
81 yield an estimated vertical resolution of c. 12 m at shallow depths, decreasing to c. 35 m towards
82 the base of supra-salt minibasins (see Appendix 1 for details). All seismic data are displayed in
83 milliseconds two-way time (ms TWT), but measurements are converted from time to depth using
84 an interval velocity of 2000 m/s. We first mapped three seismic horizons (H1–H3) to constrain salt
85 body geometry, and the 3-D distribution of throw on, and kinematics of, individual faults
86 (Appendix 2). Quantitative fault analysis was not undertaken for H1 as throw was at the limit of
87 seismic resolution (i.e. <25 m; Appendix 3). We then identified nine stratigraphic units adjacent to
88 the stock, assigning them to the two end-member CHS styles of Giles and Rowan (2012) based on
89 the width of folding and thinning, and the geometry (convergent or parallel) of the bounding
90 unconformities. These CHS allowed us to interpret periods when the rising diapir was buried by a

91 thin (tapered CHS) or thick (tabular CHS) roof (Fig. 2) (see Giles and Rowan, 2012, for recognition
92 criteria). We then grouped the units into three packages based on CHS style, and whether the stock
93 had pierced strata at the structural level of observation. Package A consists of tabular CHS, whereas
94 B and C contain tapered CHS. Packages A and B have been pierced by the salt, whereas C has not.
95 H1 lies in Package A, H2 at the boundary between A and B, and H3 in C.

96 Insert Fig. 2

97 **3. GEOLOGICAL SETTING**

98 The Santos Basin formed during Early Cretaceous rifting and initial opening of the South
99 Atlantic, during which time a thick Aptian salt layer was deposited (Ariri Formation) (Mohriak et
100 al., 2008; Contreras et al., 2010). Subsequent deposition of Albian (carbonate-dominated) and
101 Cenomanian-Holocene (siliciclastic-dominated) rocks, in addition to thin-skinned gravity-driven
102 extension, drove seaward salt flow and diapir growth (Demercian et al., 1993; Modica and Brush,
103 2004; Davison et al., 2012). We focus on a salt stock located (Fig. 1D) within the proximal,
104 extensional domain (after Davison et al., 2012), in an area unlikely to have undergone Albian
105 shortening. Like many salt structures in this area, the stock initiated as an extensional reactive
106 diapir, before undergoing passive and active rise driven by sediment loading (Jackson et al., 2015).
107 Here, we focus only on the latter stages of diapirism once the stock had developed, where CHS
108 and radial faults formed.

109 **4. SALT STOCK AND OVERBURDEN GEOMETRY, AND DIAPIRISM**

110 The salt stock is expressed in seismic data as a package of chaotic, low-amplitude reflections.
111 In cross-section, the stock is c. 4 km tall and has a ‘finger’ geometry, consisting of an up to c. 2.3
112 km wide, smooth head and stem, and a <6 km wide pedestal (Fig. 2). In plan-view, the stock is
113 sub-circular at shallow depths (c. 2000 ms TWT) and ovate at greater depths (c. 4000 ms TWT),

114 with its long axis trending NE. The presence of tabular CHS (with narrow drape folds <200 m
115 from the salt) at deeper levels indicates that, following diapir initiation, the stock entered a
116 protracted phase of passive diapirism where the volumetric flux of salt exceeded that of the
117 background sedimentation (Package A). Tapered CHS (with broad drape folds <1000 m from the
118 salt) dominate at shallower levels, suggesting sedimentation rate outpaced the volumetric flux of
119 salt (packages B and C). This could reflect an increase in the regional sedimentation rate, or a
120 decreased volumetric flux of salt as the source layer thinned and ultimately welded.

121 Shortening has been documented regionally in the Santos Basin (e.g. Demercian et al., 1993;
122 Modica and Brush, 2004; Contreras et al., 2010). However, based on the location of the stock in
123 the extensional domain (after Davison et al., 2012), the sub-circular map-view geometry (cf.
124 Jackson and Hudec, 2017), a lack of concentric thrusts in the roof (cf. Withjack and Scheiner,
125 1982; Davison et al., 2000b), and the absence of a fault-bounded ‘primary indentor’ in the putative
126 hinterland of the diapir (Dooley et al., 2009), we interpret diapir growth was *not* driven by
127 shortening. If shortening has occurred, it must be cryptic (e.g. Davison et al., 2000a; Davison et
128 al., 2000b).

129 **5. RADIAL FAULTS**

130 **Geometry and Distribution**


131 Radial faults are broadly linear in map view at all stratigraphic intervals (H1–3), although they
132 vary in their distribution, density, and length (Fig. 3). They occur over a c. 2.5 km depth range (c.
133 1–3.5 km) within tapered and tabular CHS, although they tend to cluster around the stock head in
134 tapered CHS (H2–3). It is possible that radial faults exist but are not imaged at greater depths (>3.5
135 km). Individual faults are planar, 400–1400 m tall, have aspect ratios of <2 (Appendix 4), dip at
136 50–60°, and have throws <80 m. Faults occur in vertically stacked tiers; faults within each tier

137 have similar geometric characteristics e.g. heights, lengths and densities. Largely undeformed
138 intervals define tier boundaries. Tall radial faults may cross-cut several tier boundaries and are
139 best-developed at shallower levels around the head of the stock in packages B and C (Fig. 4;
140 Appendix 5).

141 

142 **Throw Distribution**

143 We study the distribution of throw on radial faults to determine where these structures nucleated
144 with respect to the stock, which in turn, may reveal the mechanism responsible for their formation.
145 Throw maxima for faults offsetting H2–3 occur immediately at or some distance from the salt-
146 sediment interface (maximum 3 km from the stock centre; white squares on Fig. 3; Appendix 6).
147 Faults typically have ‘C-type’ throw-depth profiles (*sensu* Muraoka and Kamata, 1983), with a
148 throw maximum near their centres and very low gradients at their upper tips (<0.1) (Fig. 4A;
149 Appendix 7). Some faults may have several throw maxima separated by throw minima, and may
150 offset presumably older, neighbouring faults (Fig. 4B). Faults are not associated with growth strata
151 (expansion indices of c. 1; Fig. 4), suggesting they were blind.

152 

153 **Kinematics and Origin**

154 Based on their geometry, stratigraphic occurrence within tapered and tabular CHS, and throw
155 distribution, we propose the radial faults have two origins. Radial faults developed in the diapir
156 roof and contained in tapered CHS, with throw maxima (i.e. nucleation points; Muraoka and
157 Kamata, 1983; Baudon and Cartwright, 2008) located both above and outboard of the stock, and
158 which do not intersect the salt, formed only due to roof stretching (H3 in Fig. 3; Package C in Fig.
159 2).

160 In contrast, radial faults within tabular CHS, and which are in contact with and extend several
161 kilometres from the salt-sediment interface, that is, well beyond the limit of drape folding, formed
162 due to stem push (H1 in Fig. 3; Package A in Fig. 2). These faults nucleated at the salt-sediment
163 interface where the circumferential extension is greatest (e.g. Nikolinakou et al., 2014; Jackson
164 and Hudec, 2017). As the stock was at or near the surface with only a relatively thin roof during
165 deposition of tabular CHS, radial faults associated with roof stretching would be limited to the
166 relatively narrow extent of drape folding (<200 m), immediately adjacent to the stock. Roof
167 stretching therefore cannot be responsible for the formation of radial faults now deeply buried in
168 the stock flanks that extend kilometres away from the salt. Given the majority of deep radial faults
169 are not physically connected to shallow radial faults associated with roof stretching (Appendix 5),
170 they cannot be attributed to downward propagation of the shallower-level structures; they must
171 therefore reflect a mechanism other than drape folding. Some radial faults grew to heights of
172 several kilometres (Fig. 4), thus it is unlikely they could form due to roof stretching alone, as
173 passive diapirs driven cannot arch km-thick roofs (e.g. Davison et al., 2000b; Jackson and Hudec,
174 2017). Furthermore, given the lack of evidence for regional shortening, a mechanism that could
175 have lifted km-thick diapir roofs and generated km-tall faults, we propose such tall faults likely
176 grew due to stem push during passive diapirism (Nikolinakou et al., 2014).

177 Having considered radial faults in tabular CHS, we now explore which mechanism likely
178 produced radial faults in Package B (pierced tapered CHS). Radial faults in Package B have their
179 throw maxima either outboard of the salt or at the salt-sediment interface (H2 in Fig. 3). The former
180 suggests roof stretching must have occurred over a broad region with discontinuous faulting;
181 however, the latter could feasibly be explained by either: (i) stem push, or (ii) roof stretching, and
182 subsequent diapiric piercement of the overburden. In the first case, radial faults nucleate where

183 circumferential extension is greatest, due to stem push at the salt-sediment interface (Fig. 1B). In
184 the second case, piercement of the overburden removes sections of the roof, and portions of radial
185 faults formed by roof stretching, thus truncating the original throw distribution. Throw maxima
186 could therefore be only coincidentally located at the salt-sediment interface. Because the radial
187 faults were blind and were not associated with growth strata, we are unable to identify whether
188 stem push may have reactivated pre-existing roof stretching faults as the strata became buried (e.g.
189 Package B). Irrespective of the mechanism driving their formation, radial faults grew, dip-linked,
190 and/or offset pre-existing radial faults beside the stock (Fig. 4B) (cf. Muraoka and Kamata, 1983;
191 Baudon and Cartwright, 2008).

192 **6. DISCUSSION AND IMPLICATIONS**

193 Numerical (e.g. Yin and Groshong Jr, 2007) and physical (e.g. Parker and McDowell, 1951;
194 Withjack and Scheiner, 1982) models, maps of mined salt stocks (e.g. Barton, 1925) and exposed
195 diapirs (e.g. Powers and Hopkins, 1922; Quintà et al., 2012), and seismic reflection data (e.g.
196 Davison et al., 2000a; Stewart, 2006; Carruthers et al., 2013) provided a largely 2-D understanding
197 of radial fault geometry and growth. However, by undertaking detailed mapping of 3-D seismic
198 reflection data, we are able to not only better determine the full, 3-D geometry of *in-situ* radial
199 fault networks, but to also constrain their kinematics. Based on our observations from the Santos
200 Basin, we propose a genetic model that may be broadly applicable to other diapirs (e.g. the North
201 Sea - Davison et al., 2000; Basque-Pyrenees – Quintà et al., 2012; US Gulf Coast – Parker and
202 McDowell, 1951). We propose that, as a salt stock grows and roof thickness varies with changes
203 in the volumetric flux of salt and/or sedimentation rate, it is likely the mechanism responsible for
204 forming radial faults will vary. Such changes in the relative balance salt flux and sedimentation

205 rate may, for example, reflect progressive welding of supra-salt minibasins and/or changes in
206 regional sedimentation rate.

207 Once passive diapirism occurs and a stock starts to grow, the volumetric flux of salt may outpace
208 the background sedimentation rate, meaning the stock will be at or near the depositional surface,
209 covered only by a relatively thin roof (i.e. tabular CHS). As this thin roof is arched and is
210 shouldered aside by the rising diapir, roof stretching-related radial faults will be buried and
211 preserved immediate adjacent to (<200 m) the salt-sediment interface. As the source layer thins
212 and the volumetric flux of salt decreases, the stock may be buried by a relatively thick roof (i.e.
213 tapered CHS). Subsequent rise of the diapir generates stretching-related radial faults in the
214 aggrading overburden, over a relatively broad area (<1000 m). Shouldering aside and burial of the
215 roof along the flanks (regardless of the CHS type) may expose these strata to stem push-related
216 stresses, reactivating pre-existing or forming new radial faults. Faults in the vicinity of the salt may
217 continue to grow throughout diapirism, becoming taller and propagating laterally. Stem push-
218 related reactivation of old faults, and the formation of new faults, will be likely concentrated
219 towards the upper parts of stocks where the greatest stress perturbations occur (e.g. Fig. 8-9 in
220 Nikolinakou et al., 2014). Finally, as the salt supply is exhausted and minibasins weld,
221 sedimentation rate may outpace the volumetric flux of salt, causing stock burial (cf. Giles and
222 Rowan, 2012; Jackson and Hudec, 2017). Once diapirism ceases, no further radial faults form
223 unless latter extension or shortening occurs.

224 As the genetic mechanism for forming radial faults likely changes during diapirism, the
225 geometry and kinematics of those faults will likely change, especially where they have interacted
226 to create complex fault geometries. This could prove problematic when inverting fault network
227 geometry for paleo-stress conditions (cf. Quintà et al., 2012; Carruthers et al., 2013; Maerten et

228 al., 2016), leading to false interpretations of stress conditions, and the mode and distribution of
229 fractures around salt stocks. In addition, we highlight the structural variability and potential
230 reservoir compartmentalisation that may occur around salt stocks, providing insights into areas
231 where radial faults are not exposed or are poorly imaged (e.g. Jones and Davison, 2014).

232 **ACKNOWLEDGMENTS**

233 We thank Investigação Petrolífera Limitada (PGS) for the provision of and permission to
234 publish seismic, Schlumberger for the provision of the Petrel software licenses to Imperial College
235 London. Michael R. Hudec, Mark G. Rowan, Thilo Wrona, and Tim P. Dooley are thanked for
236 their discussions regarding passive diapirism, drape folding and faulting. Katherine Giles, Ian
237 Davison, and Stefano Tavani are thanked for their comprehensive reviews that substantially
238 improved this manuscript.

239 **REFERENCES**

- 240 Barton, D. C., 1925, The American salt-dome problems in the light of the Roumanian and German
241 salt domes: AAPG Bulletin, v. 9, no. 9, p. 1227-1268.
- 242 Baudon, C., and Cartwright, J. A., 2008, 3D seismic characterisation of an array of blind normal
243 faults in the Levant Basin, Eastern Mediterranean: Journal of Structural Geology, v. 30, no.
244 6, p. 746-760.
- 245 Carruthers, D., Cartwright, J., Jackson, M. P. A., and Schutjens, P., 2013, Origin and timing of
246 layer-bound radial faulting around North Sea salt stocks: New insights into the evolving
247 stress state around rising diapirs: Marine and Petroleum Geology, v. 48, p. 130-148.
- 248 Contreras, J., Zühlke, R., Bowman, S., and Bechstädt, T., 2010, Seismic stratigraphy and
249 subsidence analysis of the southern Brazilian margin (Campos, Santos and Pelotas basins):
250 Marine and Petroleum Geology, v. 27, no. 9, p. 1952-1980.

251 Davison, I., Alsop, G. I., Evans, N. G., and Safaricz, M., 2000a, Overburden deformation patterns
252 and mechanisms of salt diapir penetration in the Central Graben, North Sea: *Marine and*
253 *Petroleum Geology*, v. 17, no. 5, p. 601-618.

254 Davison, I., Alsop, I., Birch, P., Elders, C., Evans, N., Nicholson, H., Rorison, P., Wade, D.,
255 Woodward, J., and Young, M., 2000b, Geometry and late-stage structural evolution of
256 Central Graben salt diapirs, North Sea: *Marine and Petroleum Geology*, v. 17, no. 4, p. 499-
257 522.

258 Davison, I., Anderson, L., and Nuttall, P., 2012, Salt deposition, loading and gravity drainage in
259 the Campos and Santos salt basins: Geological Society, London, Special Publications, v.
260 363, no. 1, p. 159-174.

261 Demercian, S., Szatmari, P., and Cobbold, P. R., 1993, Style and pattern of salt diapirs due to thin-
262 skinned gravitational gliding, Campos and Santos basins, offshore Brazil: *Tectonophysics*,
263 v. 228, no. 3, p. 393-433.

264 Dooley, T. P., Jackson, M. P., and Hudec, M. R., 2009, Inflation and deflation of deeply buried salt
265 stocks during lateral shortening: *Journal of Structural Geology*, v. 31, no. 6, p. 582-600.

266 Giles, K. A., and Rowan, M. G., 2012, Concepts in halokinetic-sequence deformation and
267 stratigraphy: Geological Society, London, Special Publications, v. 363, no. 1, p. 7-31.

268 Jackson, C. A.-L., Jackson, M. P., and Hudec, M. R., 2015, Understanding the kinematics of salt-
269 bearing passive margins: A critical test of competing hypotheses for the origin of the Albian
270 Gap, Santos Basin, offshore Brazil: *Geological Society of America Bulletin*, v. 127, no. 11-
271 12, p. 1730-1751.

272 Jackson, C. A.-L., Jackson, M. P. A., Hudec, M. R., and Rodriguez, C., 2014, Internal structure,
273 kinematics, and growth of a salt wall: Insights from 3-D seismic data: *Geology*, v. 42, no.
274 4, p. 307-310.

275 Jackson, M. P., and Hudec, M. R., 2017, *Salt Tectonics: Principles and Practice*, Cambridge
276 University Press.

277 Jones, I. F., and Davison, I., 2014, Seismic imaging in and around salt bodies: *Interpretation*, v. 2,
278 no. 4, p. SL1-SL20.

279 Maerten, L., Maerten, F., Lejri, M., and Gillespie, P., 2016, Geomechanical paleostress inversion
280 using fracture data: *Journal of Structural Geology*, v. 89, p. 197-213.

281 Modica, C. J., and Brush, E. R., 2004, Postrift sequence stratigraphy, paleogeography, and fill
282 history of the deep-water Santos Basin, offshore southeast Brazil: *AAPG bulletin*, v. 88,
283 no. 7, p. 923-945.

284 Mohriak, W., Nemčok, M., and Enciso, G., 2008, South Atlantic divergent margin evolution: rift-
285 border uplift and salt tectonics in the basins of SE Brazil: Geological Society, London,
286 *Special Publications*, v. 294, no. 1, p. 365-398.

287 Muraoka, H., and Kamata, H., 1983, Displacement distribution along minor fault traces: *Journal*
288 *of Structural Geology*, v. 5, no. 5, p. 483-495.

289 Nikolinakou, M. A., Flemings, P. B., and Hudec, M. R., 2014, Modeling stress evolution around a
290 rising salt diapir: *Marine and Petroleum Geology*, v. 51, p. 230-238.

291 Parker, T. J., and McDowell, A. N., 1951, Scale models as guide to interpretation of salt-dome
292 faulting: *Geological notes: AAPG Bulletin*, v. 35, no. 9, p. 2076-2086.

293 Powers, S., and Hopkins, O. B., 1922, *The Brooks, Steen, and Grand Saline Salt Domes Smith and*
294 *Van Zandt Counties, Texas*: Washington: Government Printing Office.

295 Quintà, A., Tavani, S., and Roca, E., 2012, Fracture pattern analysis as a tool for constraining the
296 interaction between regional and diapir-related stress fields: Poza de la Sal Diapir (Basque
297 Pyrenees, Spain): Geological Society, London, Special Publications, v. 363, no. 1, p. 521-
298 532.

299 Stewart, S. A., 2006, Implications of passive salt diapir kinematics for reservoir segmentation by
300 radial and concentric faults: Marine and Petroleum Geology, v. 23, no. 8, p. 843-853.

301 Withjack, M. O., and Scheiner, C., 1982, Fault patterns associated with domes--an experimental
302 and analytical study: AAPG Bulletin, v. 66, no. 3, p. 302-316.

303 Yin, H., and Groshong Jr, R. H., 2007, A three-dimensional kinematic model for the deformation
304 above an active diapir: AAPG bulletin, v. 91, no. 3, p. 343-363.

305

306

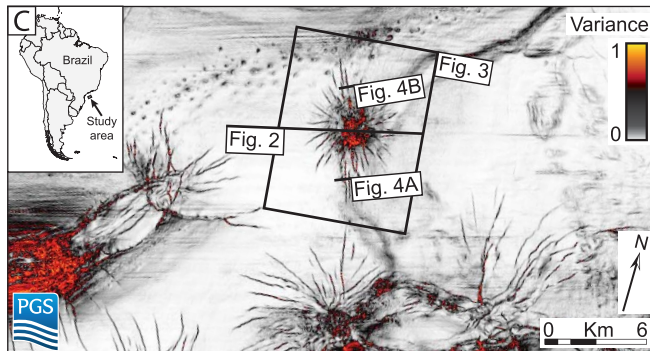
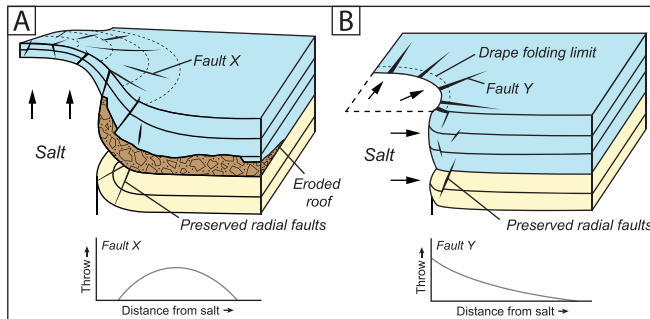
307 FIGURE CAPTIONS

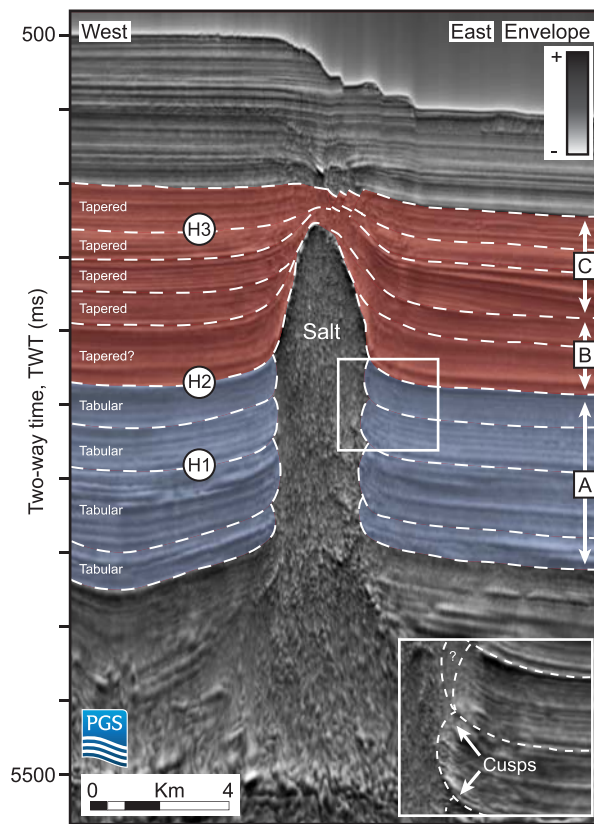
308 Fig. 1 – Formation of radial faults via roof stretching (A) and stem push (B) with idealised fault
309 throw-length plots. Radial fault Y throw increases towards the salt until it comes in contact with
310 the salt. Radial fault X does not come in contact with the salt. Geographic context and variance
311 slice at 1500 ms TWT showing the 3-D seismic extent (C). (column width figure)

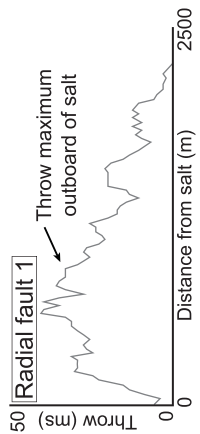
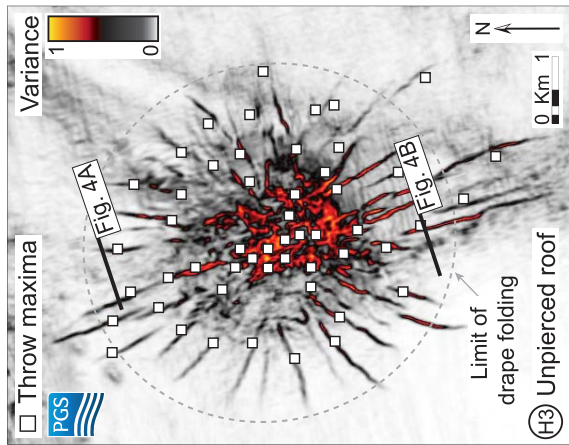
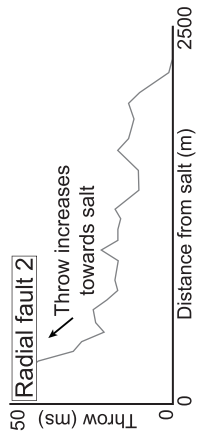
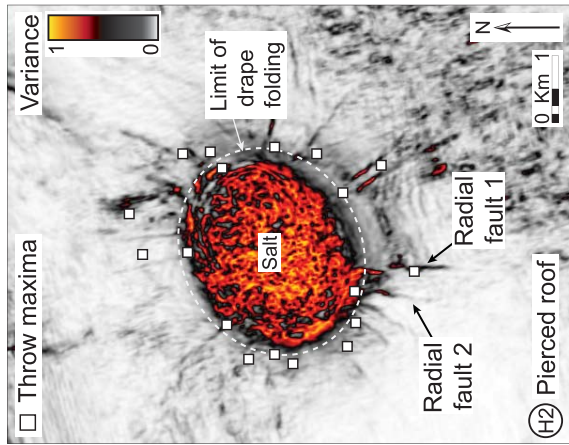
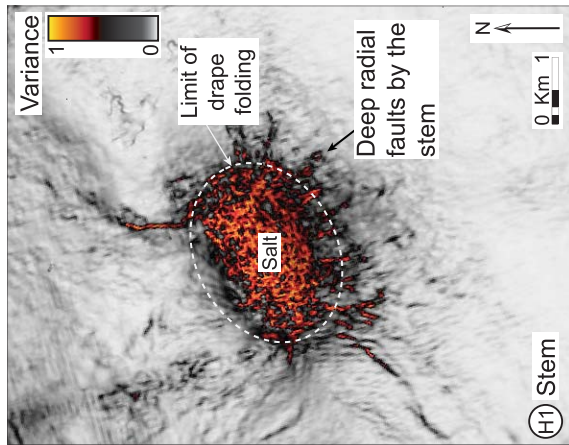
312
313 Fig. 2 – Seismic section showing the salt stock and stratigraphic position of H1–3 and packages
314 A–C. Interpreted tapered CHS – red, and tabular CHS – blue, are also shown. CHS may exhibit
315 different degrees of upturn next to the salt, forming cusps (inset). For location, see Fig. 1C. Vertical
316 exaggeration ~ 5. Seismic attribute is envelope. (column width figure)

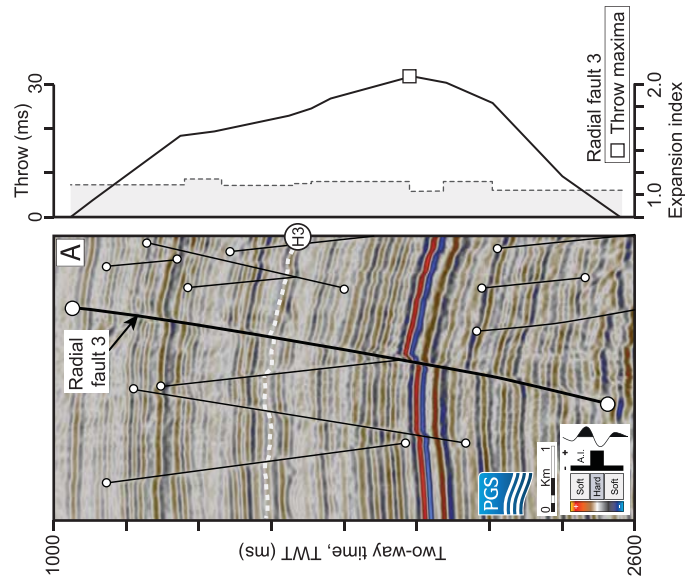
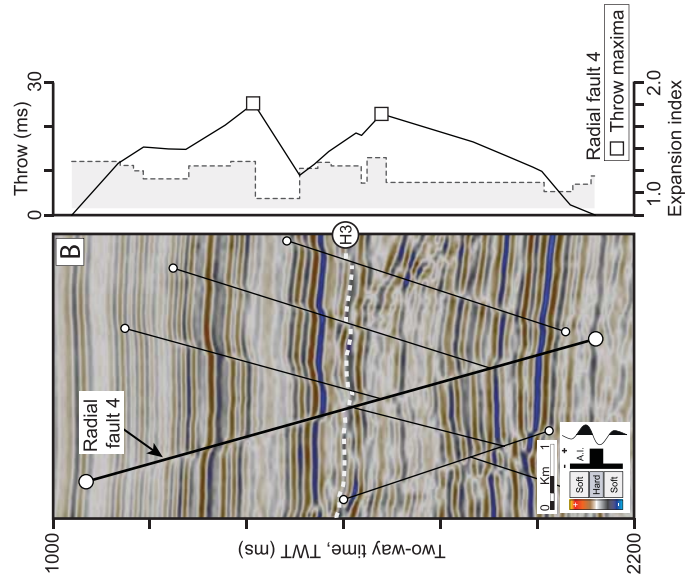
317
318 Fig. 3 – Variance attribute map for H1–3, delineating radial faults and the salt. Throw maxima
319 (white squares) for individual radial faults, throw-length plots for radial faults 1 and 2, and the
320 position of Fig. 4 are also shown. For location, see Fig. 1B. Throw maxima are absent for H1 as
321 measured throw is at the limit of seismic resolution. (two column width figure)

322
323 Fig. 4 – Radial fault 3 and 4 throw-depth profiles (solid line) and expansion indices (dashed line).
324 White circles and squares show the vertical fault tips and throw maxima, respectively. Radial fault
325 3 has a simple throw-depth profile with a single throw maximum (A). Radial fault 2 shows cross-
326 cutting of older faults (B) and two throw maxima indicative of dip linkage. Vertical exaggeration
327 ~ 5. See Fig. 3 for the location. (two column width figure)



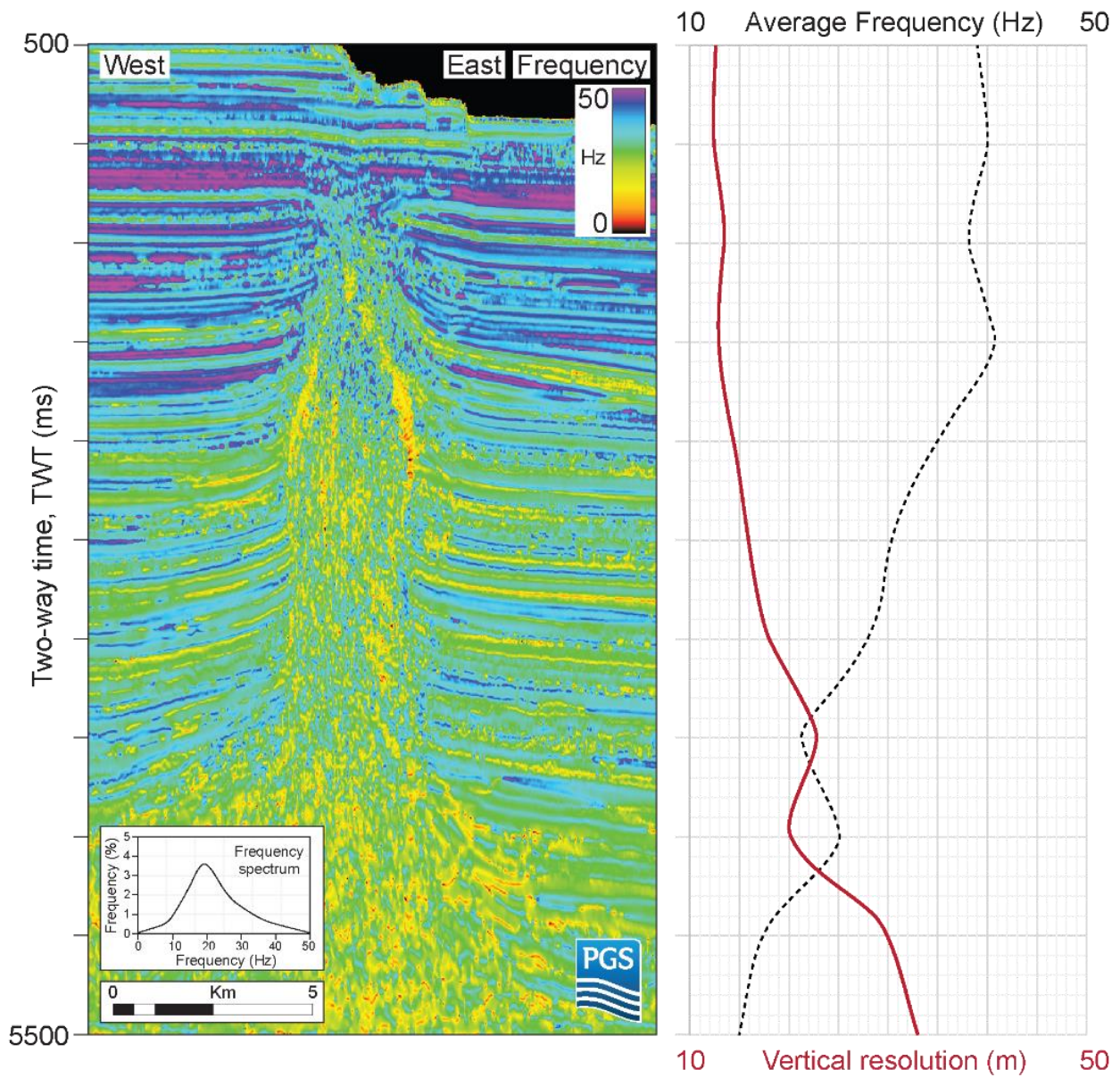






1 APPENDIX 1. AVERAGE VERTICAL SEISMIC RESOLUTION

- 2 Average vertical seismic resolution (red solid line) with depth using a velocity of ~ 2 km/s (after Jackson
- 3 et al., 2014) and the frequency (black dashed line). The average vertical seismic resolution was calculated
- 4 using the frequency and velocity. The instantaneous frequency is shown (left).

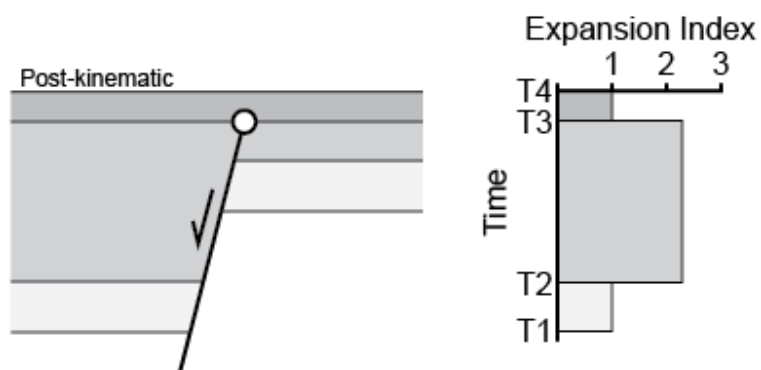
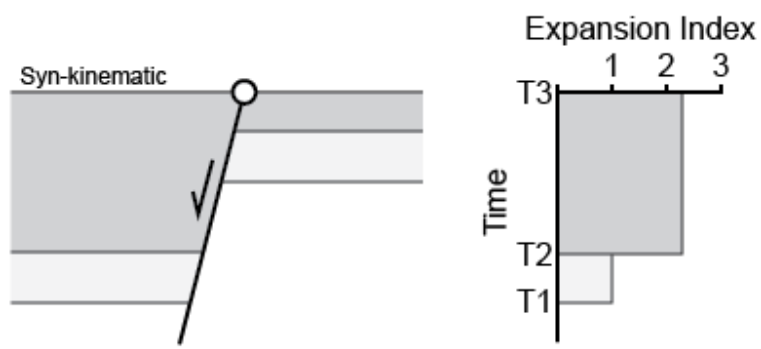
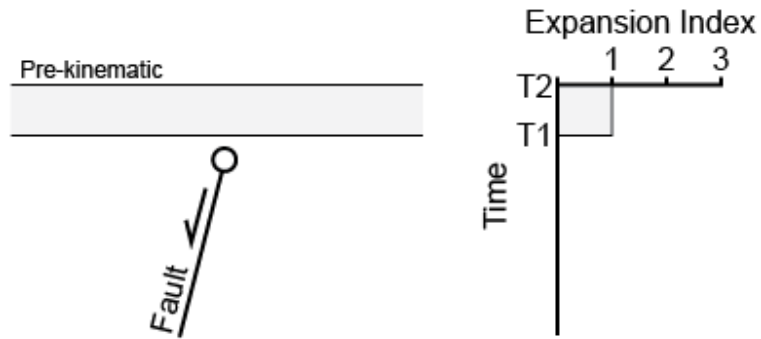
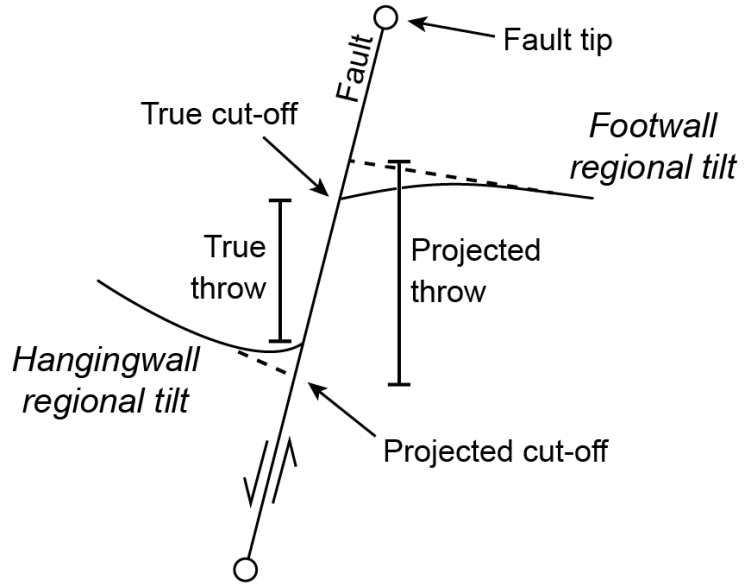


5 APPENDIX 2. QUANTITATIVE THROW ANALYSIS METHOD

6 Fault throw was measured perpendicular to radial fault strike every c. 50 – 100 m along the length of
7 individual radial faults using horizon cut-offs (e.g. Muraoka and Kamata, 1983; Baudon and Cartwright,
8 2008). Cut-offs were defined using an extrapolated line that follows the regional trend of the chosen horizon
9 prior to folding (Wilson et al., 2013), removing the effect of fault-parallel folding (Walsh et al., 1996).
10 Therefore, total strain across the fault is accommodated, whether accommodated by ductile (continuous) or
11 brittle (discontinuous) deformation (e.g. Long and Imber, 2010). The throw maxima was then identified on
12 each radial fault, and plotted as white squares on Fig. 3. Fault throw was also measured with depth (T-z
13 plots) using the aforementioned cut-offs, and throw maxima marked by white squares on Fig. 4.

14 Expansion indices illustrate variations in sediment thickness adjacent to fault systems, revealing the
15 kinematics of bounding faults (e.g. Thorsen, 1963; Tvedt et al., 2013; Jackson et al., 2017). Expansion
16 indices were calculated by dividing the hangingwall thickness of a stratal units by its corresponding footwall
17 thickness and plotting these against geological time. An expansion index of 1 suggests no across-fault
18 thickening, and a lack of syndepositional fault activity. An index of >1 suggests across-fault thickening and
19 syndepositional fault activity. An index of <1 suggests stratal thinning from the footwall to the hangingwall,
20 and may reflect difficulties in accurately measuring stratal thicknesses adjacent to a fault. Expansion indices
21 near vertical fault tips may be slightly above and below one (± 0.1) due to ductile deformation (e.g. Barnett
22 et al., 1987). T1 – T4 represent horizon tops. The white circle represents the vertical fault tip.

23



25 References for Appendix 2

- 26 Barnett, J. A., Mortimer, J., Rippon, J. H., Walsh, J. J., and Watterson, J., 1987, Displacement
27 geometry in the volume containing a single normal fault: AAPG Bulletin, v. 71, no. 8, p.
28 925-937.
- 29 Baudon, C., and Cartwright, J. A., 2008, 3D seismic characterisation of an array of blind normal
30 faults in the Levant Basin, Eastern Mediterranean: Journal of Structural Geology, v. 30,
31 no. 6, p. 746-760.
- 32 Jackson, C. A.-L., Bell, R. E., Rotevatn, A., and Tvedt, A. B. M., 2017, Techniques to determine
33 the kinematics of synsedimentary normal faults and implications for fault growth models:
34 Geological Society, London, Special Publications, v. 439.
- 35 Long, J., and Imber, J., 2010, Geometrically coherent continuous deformation in the volume
36 surrounding a seismically imaged normal fault-array: Journal of Structural Geology, v. 32,
37 no. 2, p. 222-234.
- 38 Muraoka, H., and Kamata, H., 1983, Displacement distribution along minor fault traces: Journal
39 of Structural Geology, v. 5, no. 5, p. 483-495.
- 40 Thorsen, C. E., 1963, Age of growth faulting in southeast Louisiana.
- 41 Tvedt, A. B. M., Rotevatn, A., Jackson, C. A. L., Fossen, H., and Gawthorpe, R. L., 2013, Growth
42 of normal faults in multilayer sequences: A 3D seismic case study from the Egersund
43 Basin, Norwegian North Sea: Journal of Structural Geology, v. 55, p. 1-20.
- 44 Walsh, J. J., Watterson, J., Childs, C., and Nicol, A., 1996, Ductile strain effects in the analysis of
45 seismic interpretations of normal fault systems: Geological Society, London, Special
46 Publications, v. 99, no. 1, p. 27-40.

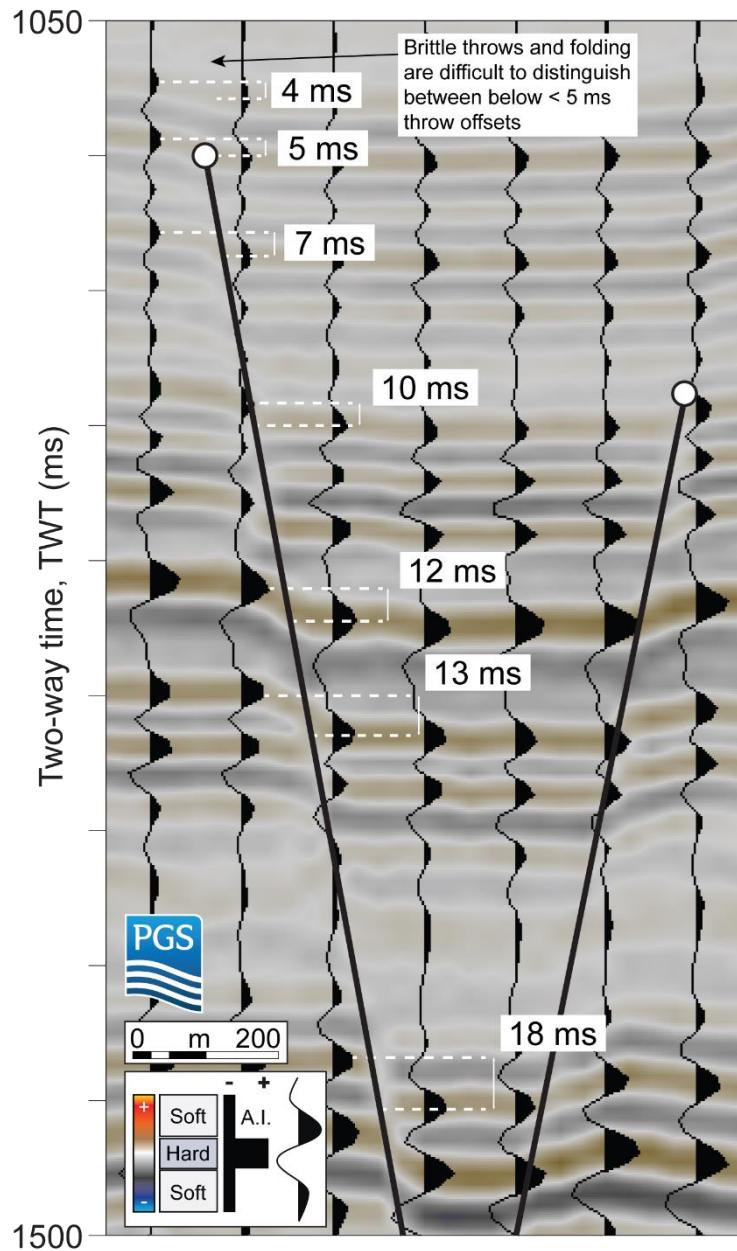
47 Wilson, P., Elliott, G. M., Gawthorpe, R. L., Jackson, C. A.-L., Michelsen, L., and Sharp, I. R.,
48 2013, Geometry and segmentation of an evaporite-detached normal fault array: 3D seismic
49 analysis of the southern Bremstein Fault Complex, offshore mid-Norway: Journal of
50 Structural Geology, v. 51, p. 74-91.

51

52 APPENDIX 3. FAULT THROW RESOLUTION

53 Fault throw resolution for an example radial fault at Santos. Although vertical resolution may decrease with
54 depth, the vertical offset between amplitude peaks between adjacent seismic traces permits fault throw to
55 be measured to c. 5ms at shallow depths (< 3000 ms TWT). However, at greater depths (>3000 ms TWT),
56 the peaks of individual traces become increasingly smeared as the vertical resolution decreases, and as such,
57 vertical offsets are less distinct and measurement becomes increasingly difficult.

58



59 APPENDIX 4. ASPECT RATIO FOR SANTOS BASIN RADIAL FAULTS

60 Aspect ratios for Santos Basin radial faults. Velocity ~ 2km/s after Jackson et al. (2014).

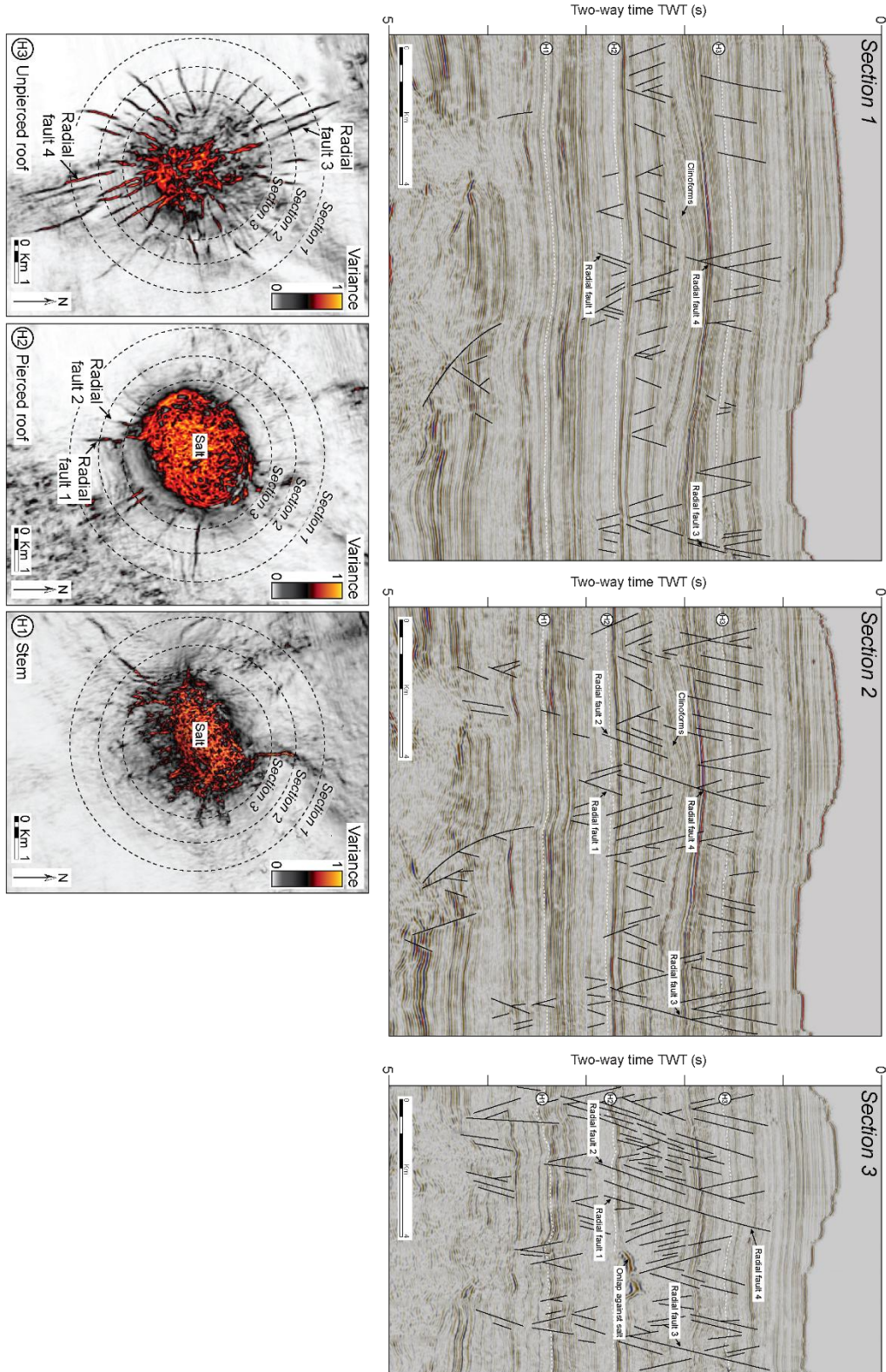
Fault #	Max Length (m)	Height (m)	Aspect Ratio
1	3727	871	4.28
2	704	596	1.18
3	639	639	0.69
4	2021	811	2.49
5	1340	809	1.66
6	1131	655	1.73
7	601	361	1.66
8	2909	1521	1.91
9	1075	434	2.48
10	1732	650	2.66
11	644	557	1.16
12	1536	923	1.66
13	833	833	0.72
14	1542	620	2.49
15	1826	683	2.67
16	1100	208	5.29
17	1742	666	2.62
18	1322	500	2.64
19	2001	736	2.72
20	809	545	1.48
21	579	579	0.78
22	1246	275	4.53
23	1969	501	3.93
24	947	323	2.93
25	2585	676	3.82
26	882	735	1.20
27	1726	669	2.58
28	1490	731	2.04
29	1713	368	4.65
30	600	580	1.03
31	1146	663	1.73
32	644	579	1.11
33	1471	782	1.88
34	1004	350	2.87
35	412	412	0.90
36	754	496	1.52
37	903	670	1.35
38	2510	401	6.26
39	1457	693	2.10
40	464	464	0.82
41	726	726	0.52

42	540	540	0.92
43	955	685	1.39
44	856	657	1.30
45	1328	493	2.69
46	1072	734	1.46
47	791	726	1.09
48	1619	566	2.86
49	1580	551	2.87
50	1276	707	1.80
51	1288	463	2.78
52	859	701	1.23
53	1764	699	2.52
54	1090	480	2.27
55	964	596	1.62
56	754	754	0.88

62 APPENDIX 5. CIRCUMFERENTIAL SEISMIC SECTIONS

63 Circumferential seismic sections parallel to the salt-sediment interface documenting the different vertical
 64 tiers of radial faults around the isolated salt stock. H1 – 3 and Faults 1 - 4 are also shown.

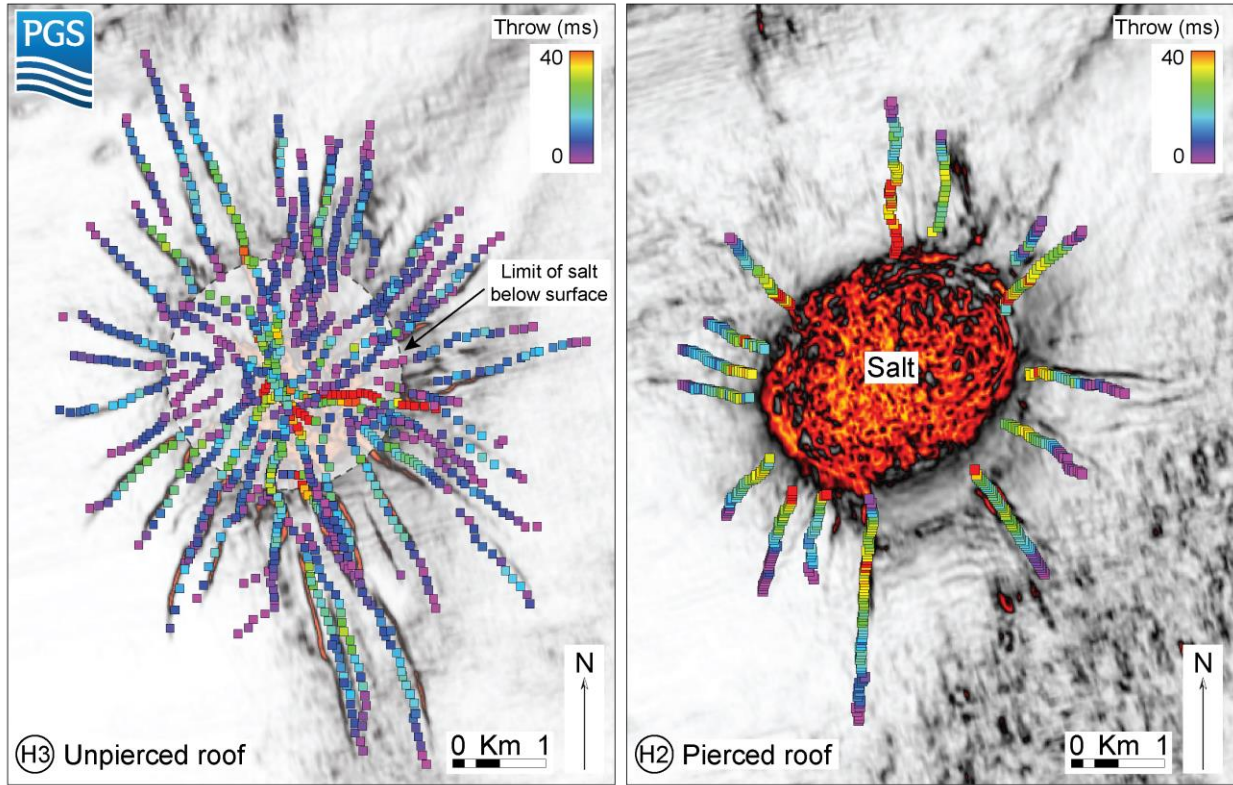
65



66 APPENDIX 6. RADIAL FAULT THROW FOR H2-3

67 Throw-distance on Fig. 3 used to determine the position of throw maxima along-strike for H2 - 3. Radial

68 fault throw (i.e. strain) generally increases towards the diapir in H1 and H2.



69 APPENDIX 7. UPPER THROW TIP GRADIENTS

70 Upper throw tip gradients for the Santos Basin radial faults.

Fault	Throw (m)	Upper tip radius (m)	Vertical tip throw gradient
1	47	494	0.09
2	32	308	0.10
3	25	350	0.07
4	25	281	0.09
5	25	202	0.12
6	20	139	0.14
7	26	197	0.13
8	23	499	0.05
9	23	233	0.10
10	21	303	0.07
11	36	322	0.11
12	37	507	0.07
13	21	123	0.17
14	16	151	0.11
15	15	66	0.23
16	29	254	0.11
17	38	368	0.10
18	30	307	0.10
19	24	126	0.19
20	20	338	0.06
21	20	147	0.14
22	20	305	0.07
23	20	469	0.04
24	20	454	0.04

25	66	515	0.13
26	60	499	0.12
27	22	125	0.18
28	22	206	0.11
29	23	310	0.07
30	22	427	0.05
31	21	312	0.07
32	19	231	0.08
33	19	194	0.10
34	22	396	0.06
35	24	250	0.09
36	21	335	0.06
37	14	284	0.05
38	18	247	0.07
39	21	248	0.08
40	18	337	0.05